RSC Advances

PAPER

View Article Online
View Journal | View Issue

Cite this: *RSC Adv.*, 2026, **16**, 17337

Phytogenic silver nanoparticles synthesized from *Dendrophthoe falcata* and *Ocimum tenuiflorum*: SERS and ultrafast nonlinear optical studies

Jhansi Mogilipuri,[a] Srilakshmi P. Bhaskar,[b] Venugopal Rao Soma *[c] and Sabitha Mohan *[a]

The surface enhanced Raman scattering (SERS) performance and femtosecond third-order nonlinear optical (NLO) properties of green synthesized silver nanoparticles (AgNPs) were systematically investigated in this work. Three dye molecules (nile blue-NB, crystal violet-CV and methylene blue-MB) and an explosive molecule (picric acid-PA) were utilized as probe analytes for the SERS detection. Among the different plant mediated syntheses, AgNPs synthesized with Dendrophthoe falcata plant extract (AgL) demonstrated a superior SERS enhancement (~10^6) with high signal reproducibility and sensitivity. With AgL as the SERS substrate, the detection sensitivity of NB, PA, MB, and CV were measured to be 10 nM, 10 μM, 100 nM and 50 μM, respectively, with Raman enhancement factors ranging from 10^3 to 10^6. In contrast, AgNPs synthesized with Ocimum Tenuiflorum (AgT) depicted one order lower SERS enhancement, with reduced signal reproducibility. Fourier Transform Infrared (FTIR) spectroscopy was utilized to examine the phytochemical composition of plant extracts used for synthesis. Transmission electron microscopy (TEM) analysis of AgL reveals nearly spherical-nanoparticles with a narrow size distribution (3–10 nm); while AgT displayed large nanoparticles with significant variation in size (10–70 nm) and shape (aspect ratio of ~0.9–2). COMSOL Multiphysics simulation based on the finite element method was implemented to investigate the correlation between nanoparticle morphology (AgL and AgT) and the associated electric field enhancements. Furthermore, femtosecond Z-scan experiments were performed on AgL and AgT samples and their optical nonlinearity is found to be dominated by a two-photon process, which can be tailored to meet specific NLO applications. These results highlight the crucial role of green AgNPs mediated *via* plant-derived agents in tuning nanoparticle morphology and plasmonic behaviour, hence offering an efficient green route to enhance the performance of SERS substrates as well as for NLO applications.

Received 1st January 2026
Accepted 18th March 2026

DOI: 10.1039/d6ra00003g

rsc.li/rsc-advances

1 Introduction

Metal nanoparticles have gained special attention due their exceptional plasmonic properties, particularly, known as localized surface plasmon resonance (LSPR).[1–4] At LSPR frequency, the incident electromagnetic radiation induces collective oscillations, resulting in an amplification of electric field in the vicinity of the nanoparticle surface, which makes them ideal candidates for optical sensing and nonlinear optical applications.[5,6] The formation of electromagnetic hotspots in the neighbourhood of the nanoparticle can be precisely tailored by controlling the nanoparticle size, shape and inter-particle distance to obtain an electric-field enhancement of considerable extent.[7,8] Surface-enhanced Raman scattering/spectroscopy (SERS) is a highly sensitive analytical technique that exploits the LSPR of noble metal nanoparticles to amplify Raman signals, enabling ultra-sensitive detection of biomolecules, environmental pollutants, explosives and pathogens.[9–13] Typically, in SERS, the amplification of the Raman signal originates mainly from electromagnetic enhancement which involves plasmonic coupling among the metal nanoparticles that generates amplified electromagnetic field or hot spots.[7,8] Among various plasmonic materials, silver nanoparticles (AgNPs) have gained a particular attention due to its strong and tunable-localized plasmon resonance (LSPR) coupled with low intrinsic losses. The ability of AgNPs to enhance the Raman signal in the electromagnetic field is reported to be 2–3 times higher than that of gold, making them ideal substrates for molecular fingerprinting at trace levels.[14,15]

Conventional techniques of AgNPs synthesis typically involve chemical and physical techniques that often require toxic

[a]*Department of Physical and Chemical Sciences, Sri Sathya Sai University for Human Excellence, Navanihal, Kalaburagi, Karnataka 585313, India. E-mail: sabitha.m@sssuhe.ac.in*

[b]*Department of Chemistry, Vimala College (Autonomous), Thrissur, Kerala 680009, India*

[c]*School of Physics and DIA-CoE (formerly ACRHEM), University of Hyderabad, Hyderabad 500046, India. E-mail: soma_venu@yahoo.com*

reducing agents and high energy inputs, raising environmental as well as biocompatibility concerns.[16,17] On contrary, green synthesis strategies involving plant mediated bio-synthesis, have emerged as sustainable alternatives for nanoparticles production. Phytochemicals in plant extracts play a vital role in the green synthesis of silver nanoparticles (AgNPs) serving as both reducing agents that convert silver ions (Ag^{+}) to metallic silver (Ag^{0}) and also as stabilizing or capping agents that control nanoparticle growth and prevent aggregation.[17–19] Thus, the morphology of the nanoparticles such as size, shape, and the surface chemistry of the nanoparticles depends upon the chemical composition of phytochemicals present in the leaf extracts. Phytochemical composition in different plant species offer varied reducing and stabilizing capabilities, leading to diverse nanoparticle morphologies such as spherical, rod-like, or hexagonal structures and influencing their overall properties and stability.[18–20]

In the recent years green AgNPs have extensively explored for anti-microbial activities, catalytic and anti-cancer applications. However, their application as SERS substrate is very limited.[21–24] Among the reported works, Mazali *et al.* have demonstrated the detection of analyte molecules such as 4 aminobenzenethiol, Rhodamine 6G, and methylene blue using the self-assembly of green AgNPs reduced with citrus plant extract. While Jaiswal-Nagar *et al.* reported the detection of Crystal violet molecule with green AgNPs mediated *via* Christ throne plant extract. The work of Cortez-Valadez *et al.* have demonstrated the detection of pyridoxine molecules upon using green AgNPs reduced with leaves, and stem extracts of the Bougainvillea spectabilis.[25–27] In this context, the present work demonstrates the detection of Nile Blue (NB), a highly toxic, textile dye which is carcinogenic in nature, posing a significant threat into environment and human health.[28] Also, the detection of picric acid (PA), an explosive molecule, highly unstable, toxic with carcinogenic characteristics, as probe analyte by employing green synthesised AgNPs as the SERS substrate.[29] To the best of our knowledge, no prior work has reported on the detection of NB and PA by using the green synthesized AgNPs, as a SERS substrate. Furthermore, the versatility of green AgNPs based SERS substrate is established through the detection of additional two dye molecules including Methylene Blue (MB) and Crystal Violet (CV).

This work also examines how the phytochemical composition of leaf extracts of different plants influences the microscopic morphology of AgNPs, which is a crucial parameter in determining SERS activity. In this context we have synthesized AgNPs using two different plants (i) *Dendrophthoe falcata* and (ii) *Ocimum tenuiflorum*. These two different plant extract exhibit markedly different phytochemical compositions, leading to distinct nanoparticle morphologies and plasmonic responses. *Dendrophthoe falcata* (*D. falcata*) belongs to the species of *Loranthaceae* family, whose phytochemical investigations reported the presence of diverse classes of bioactive compounds including quercetin, quercitrin, rutin, gallic acid, β-amyrin acetate, and β-sitosterol flavonoids, triterpenes, tannins, steroids, open-chain aliphatic compounds, benzyl derivatives, and cyclic chain derivatives.[30,31] While *Ocimum tenuiflorum* (*O. tenuiflorum*), known as *Tulsi*, contains several bioactive constituents including ocimol, galactose, arabinose, β-sitosterol, ocimic acid, ursolic acid, trihydroxy ursolic acid, palmityl glucoside, menthylsalicylic glucoside, and capryl tetra glycosidic salicylate.[32–34] Accordingly, the AgNPs synthesized with *D. falcata* is labelled as AgL and that derived from *O. tenuiflorum* is labelled as AgT.

By employing COMSOL Multiphysics software based on Finite Element Method (FEM), the dependence of morphology on electric field enhancement of AgL and AgT substrate was calculated. In addition to their SERS studies, the investigations into ultrafast optical nonlinearities of AgL and AgT by utilizing a femtosecond Z-scan technique were carried out, which reveals the NLO properties of green AgNPs can be tailored to meet the photonic applications based on two-photon absorption process. Thus, our work demonstrates that, the integration of green-synthesized AgNPs into SERS and NLO platforms not only enhances detection sensitivity but also provide plasmonic based photonic devices which aligns with sustainable green nanotechnology.

2 Experimental section

2.1 Materials

D. falcata leaves were obtained from Thrissur, Kerala and *O. tenuiflorum* locally known as *Tulasi* leaves were sourced from Nallakadirinahalli, Karnataka. Silver nitrate ($AgNO_3$, 99.9%), from Merck AR grade, Picric acid (PA) was procured from HEMRL (Pune, India), nile blue (NB), crystal violet (CV) and methylene blue (MB) were procured from commercial sources. All reagents were used without further purification. Stock solutions of PA, NB, CV and MB were prepared separately by dissolving them in double deionized (DI) water, which was used as the solvent for all preparations. Prior to use, all glassware was meticulously cleaned using a sonication process, followed by a final rinse with distilled water.

2.2 Synthesis of silver nanoparticles (AgNPs)

Green synthesis of AgNPs was carried out separately using *D. falcata* and *O. tenuiflorum* leaf extracts following a similar procedure described in (ref. 35). The collected leaves were thoroughly washed four times with DI water and shade-dried. The dried leaves were subsequently finely powdered and 10 grams of the powdered leaves mixed with 200 mL DI water were boiled for 30 minutes. The extract was then cooled down to room temperature and filtered using Whatman filter paper to obtain the clarified solution. Two batches of 0.01 M aqueous solution of $AgNO_3$ were prepared by dissolving silver nitrate in 20 mL of distilled water. Then, 5 mL of each leaf extract was then added slowly to the silver nitrate solution under continuous stirring for 2 h at room temperature. Upon addition of *D. falcata* leaf extract, a rapid colour change to dark yellowish brown was observed while *O. tenuiflorum* results a dark brown colour, indicating the formation of AgNPs. The resulting AgNPs were further diluted, displaying a characteristic golden-yellow colour, confirming the presence of nanoparticles. The synthesized AgNPs solutions were stored at 4 °C until further analysis.

2.3 Instrumentation

The optical absorption of green AgNPs system were measured using a UV-visible spectrometer (JASCO V-670) in the wavelength range of 300–800 nm with a resolution of 0.5 nm. Morphology features of nanoparticles were analysed using Transmission Electron Microscopy [JEM-2100F; JEOL, Japan]. The size distribution and shape of the nanoparticles were analysed using ImageJ software. X-ray Diffraction (XRD) analysis was performed to examine the crystallinity and phase purity of the synthesized silver nanoparticles (Rigaku Mini Flex 300/600 diffractometer equipped with a Cu-Kα radiation source, operating in θ–2θ configuration). FTIR spectroscopy was conducted to identify the functional groups responsible cfor reduction and stabilization of the AgNPs. The finely powdered dried plant extract were mixed with spectroscopic grade KBr and pressed into pellets. Spectra were recorded using a PerkinElmer Spectrum (Diamond/ZnSe, PIKE Technologies, Serial No. 22095). The optical emission properties of the AgNPs were recorded (Fluorolog® Horiba Jobin Yvon spectrophotometer). SERS measurements were performed using LabRAM HR Evolution (Horiba, Japan) equipped with a 633 nm excitation laser source. A 50× objective lens was used to focus the laser on the sample. The nonlinear optical (NLO) characteristics of AgL and AgT are measured using the femtosecond Z-scan measurements.

3 Results and discussion

3.1 UV-visible absorption spectra

Silver nanoparticles (AgNPs) were successfully synthesized using *D. falcata* and *O. tenuiflorum* extracts as bio-reducing agents. The formation of AgNPs was initially confirmed by a colour change of colloidal solution from light brown to the dark yellowish brown. Further, the nanoparticle solution of AgL and AgT is diluted as well as sonicated to eliminate the possibility of any nanoparticle agglomeration. The concentration of nanoparticle is adjusted such that the linear absorption coefficient of nanoparticle solution at LSPR wavelength was 6.91 cm^{-1}. The UV-visible absorption spectra of green AgNPs and the corresponding leaf extract are shown in Fig. 1(a) and (b). The AgNPs synthesized with *D. falcata* extract (AgL) exhibited a localized surface plasmon resonance (LSPR) peak at 427 nm, whereas those synthesized with *O. tenuiflorum* extract (AgT) depicted the LSPR peak at 444 nm.

The absorption spectra of the leaf extracts of *D. falcata* as well as *O. tenuiflorum* does not exhibit any features in the spectral range of interest. The blueshift in LSPR peak position of AgL in-comparison to AgT indicates the formation of smaller NPs with *D. falcata* compared to *O. tenuiflorum* mediated synthesis. Additionally, the bandwidth of AgL (FWHM of ~92 nm) was found to be relatively narrower compared to that of AgT (FWHM of ~153 nm) indicating a more uniform size and shape distribution for AgL nanoparticles.[1,2]

3.2 TEM analysis

The transmission electron microscope (TEM) analysis was employed to study the morphological differences between the green AgNPs of AgT and AgL. Fig. 2(a)–(c) depict the TEM images of AgT NPs recorded at different magnifications, illustrating relatively larger, polydisperse nanoparticles with sizes ranging from 12–70 nm; in contrast, Fig. 2(d)–(f) illustrate that the nanoparticles of AgL were significantly smaller, spherical and more uniformly distributed having size range of 3–10 nm. Histogram representing the size and shape distribution of AgT NPs calculated from TEM monograph (Fig. S1(a): SI data) are shown in Fig. 2(g) and (h), where the shape of the nanoparticle is denoted by its aspect ratio (ratio of particle axial length, as shown in inset).

The aspect ratio value ranges from 0.9 to 2, indicating a wide shape distribution spanning from oblate to prolate spheroids.[1–3] Respective histogram plot in Fig. 2(h) shows approximately 60% are of spherical and remaining 40% exhibit non-spherical morphology. In contrast, for AgL NPs, histogram [TEM monograph, Fig. S1(b)] as shown in Fig. 2(i) indicates narrow size distribution with a fine uniformity in shape of the nanoparticles, demonstrating more controlled growth and shape homogeneity in *D. falcata* mediated synthesis.

3.3 XRD analysis

The crystalline structure and phase purity of the biosynthesized silver nanoparticles (AgNPs) were analysed using X-ray diffraction (XRD). As illustrated in Fig. 3(a), the XRD patterns

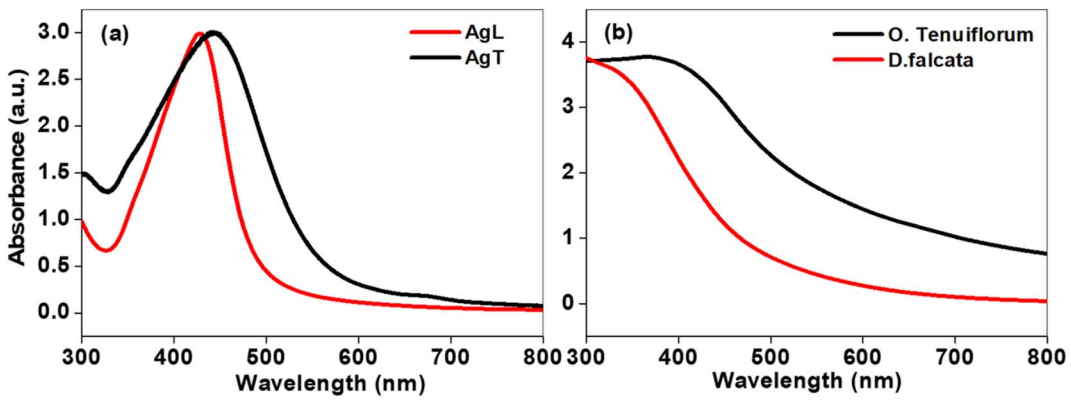

Fig. 1 (a) UV-visible absorption spectra of AgL and AgT nanoparticles and (b) absorption spectra of *D. falcata* and *O. tenuiflorum* leaf extracts.

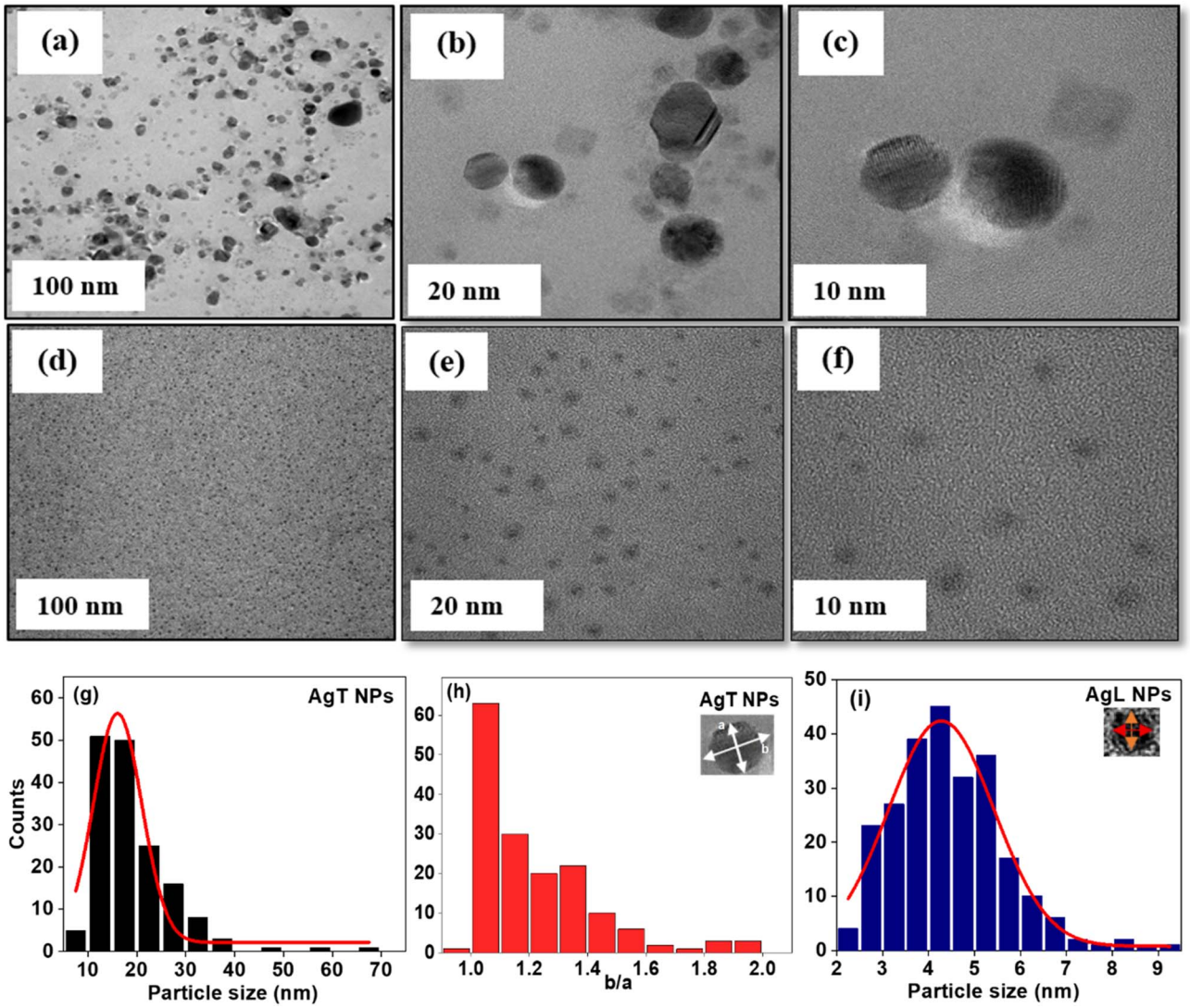

Fig. 2 (a–c) Represents the TEM images of AgT NPs at various magnifications (100 nm, 20 nm, and 10 nm respectively); (d–f) represents that of AgL NPs; and (g)–(h) denotes the size and shape (b/a) distribution of AgT NPs while (i) represents the size distribution of AgL NPs.

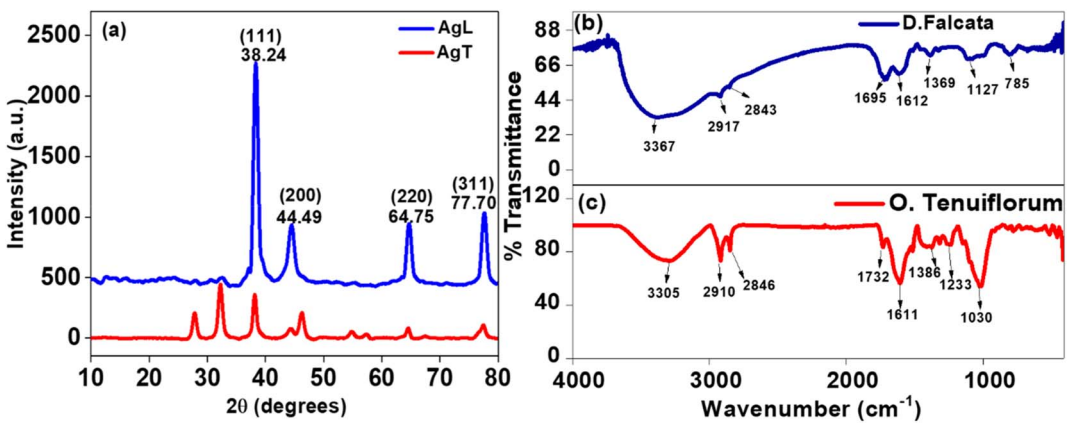

Fig. 3 (a) X-ray diffraction (XRD) patterns of AgL and AgT NPs, (b) and (c) FTIR spectra of *Dendrophthoe falcata* and *Ocimum Tenuiflorum* leaf extracts.

of green synthesised AgNPs revealed distinct differences in crystallinity. Both samples exhibit characteristic diffraction peaks at 2θ values of 38.24°, 44.49°, 64.75°, and 77.70° corresponding to the (111), (200), (220), and (311) crystallographic planes of face-cantered cubic (FCC) silver, JCPDS No. 04-0783 confirming the peaks of metallic silver nanoparticles in both cases.[36,37]

However, the relative intensity of these peaks is significantly higher for the AgL sample indicating a higher degree of polycrystallinity and greater particle density compared to AgT. In contrast, the XRD of AgT displays additional low-intensity peaks centred at 27.73° and 32.21° indicates the formation of AgCl phase [JCPDS No. 31-1238], which may form due to the interaction of silver ions with chloride-containing phytochemicals naturally present in the *O. tenuiflorum* extract. The presence of AgCl peaks suggests partial conversion of Ag^+ to AgCl during the green synthesis process of AgT.[38,39]

3.4 FTIR spectral analysis

The FTIR spectra of *D. falcata* and *O. tenuiflorum* leaf powder, presented in Fig. 3(b) and (c) reveal several common functional groups, indicating the presence of similar classes of bioactive compounds. Both indicates the presence of aromatic compounds such as flavonoids and tannins. Wavenumber range and corresponding functional group obtained from transmittance spectra are presented in Table 1.[34,40] Although both leaf extracts illustrate similar key FTIR features, *D. falcata* shows comparatively broader primary band around 3367 cm^{-1}, in-comparison to *O. tenuiflorum* indicating its higher chemical complexity. This broader band indicates higher varieties and abundance of phytochemicals in *D. falcata* making it a potentially superior source of natural reducing and capping agents in the green synthesis process. Consequently, rich phytochemical content in *D. falcata* plausibly encapsulate the AgNPs efficiently there by restricting the further growth and yielding smaller sized AgL NPs. While a moderate concentration of phytochemicals in *O. tenuiflorum* may favours a growth mediated mechanism permitting an extended particle growth.[41,42]

3.5 Photoluminescence analysis

Photoluminescence (PL) spectroscopy was employed to analyse the optical emission characteristics of the green AgNPs and corresponding leaf extracts. The PL spectra were recorded at excitation wavelengths of 330 nm for AgL (*D. falcata*) and 400 nm for AgT (*O. tenuiflorum*). As illustrated in Fig. 4(a), the AgL exhibited a broad emission band centred on 456 nm, whereas the emission of *D. falcata* extract is observed at 450 nm. In comparison, as shown in Fig. 4(b), the AgT nanoparticles displayed a prominent emission peak around 463 nm, with emission of *O. tenuiflorum* around 469 nm. The observed PL emission in AgL at 330 nm excitation is likely arising from the excitation of electrons from occupied d-bands to sp-band, followed by electron–hole recombination.[43,44] In the case of AgT NPs, emission under 400 nm excitation, is plausibly attributed to the radiative relaxation of LSPR from excited state to the ground state. The observed blue shift in PL emission of AgL NPs in comparison to AgT NPs further reflects the size dependent nature of PL; *i.e.*, AgL having smaller sized nanoparticles depicting a blue shifted emission due to interband transition, and subsequent relaxation, in contrast to radiative decay of LSPR in relatively large sized AgT NPs.[43,44] Additionally, the PL emission of leaf extract is believed to be primarily arising from presence of fluorophores in phytochemicals such as flavonoids and phenolic compounds.[45]

4 Evaluation of SERS activity of AgL and AgT nanoparticles

The Raman/SERS spectra were recorded with AgNPs drop casted onto silicon wafers using a Lab RAM Horiba Raman Spectrometer with a 633 nm laser excitation source. All the SERS spectra are presented in Fig. 5(a)–(i). As shown in Fig. 5(a), the Raman spectra of the bare AgL and AgT did not exhibit any intrinsic Raman peak at the spectral range of interest. The peak observed at 520 cm^{-1} is found to be the characteristic phonon mode of silicon (Si) substrate. The SERS substrates are prepared by drop casting AgNPs solution on to clean Si wafers, followed by drop casting the analyte molecules. Fig. 5(b)–(i) depict the SERS activity of AgL and AgT substrates evaluated using three dye molecules NB, MB, CV and an explosive molecule PA.

The SERS measurement of NB using AgL as substrate at concentrations of 500 μM, 100 μM and 10 μM are shown in Fig. 5(b), which clearly depicts an increase in Raman peak intensity with increase of NB concentration. The characteristic

Table 1 FTIR peaks and corresponding functional groups of leaf extracts of plants *D. falcata* and *O. tenuiflorum*

Functional group	Compound	Frequency range [cm^{-1}]	*Dendrophthoe falcata* [cm^{-1}]	*Ocimum tenuiflorum* [cm^{-1}]
O–H stretch	Alcohol	3550–3200	3367 (broad)	3305
C–H stretch	Alkane	3000–2840	2917, 2843	2910, 2846
C=O stretch	Aldehydes, ketones, esters, carboxylic acids, anhydrides	1830–1650	1695	1732
C=C stretch	Alkene, α, β ketone	1662–1610	1612	1611
O–H bending	Aliphatic amines	1420–1330	1369	1386
C–N stretch	Aliphatic amines	1250–1020	1127	1233
S=O stretch	Sulfoxide	1070–1030	—	1030
C–H bending	1, 2, 3-tridistributed	780 ± 20	785	—

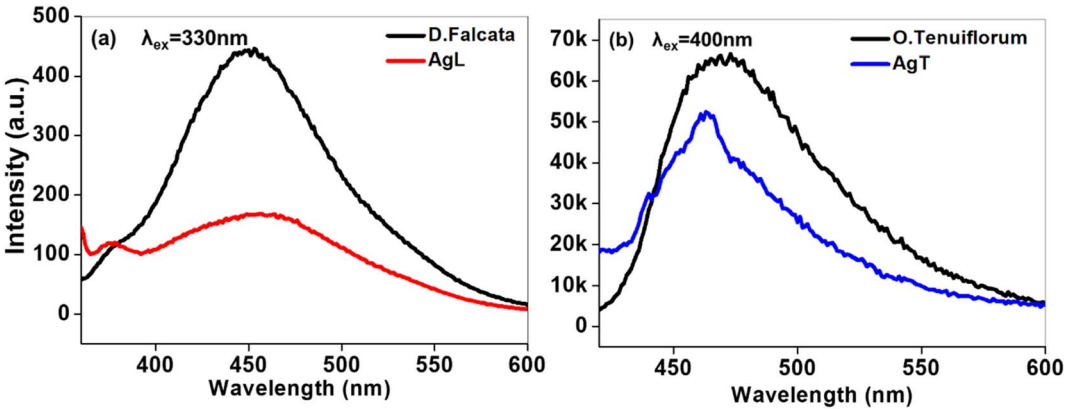

Fig. 4 (a) PL spectra of AgL and *D. falcata* extract at 330 nm excitation and (b) PL spectra of AgT and *O. tenuiflorum* at 400 nm excitation.

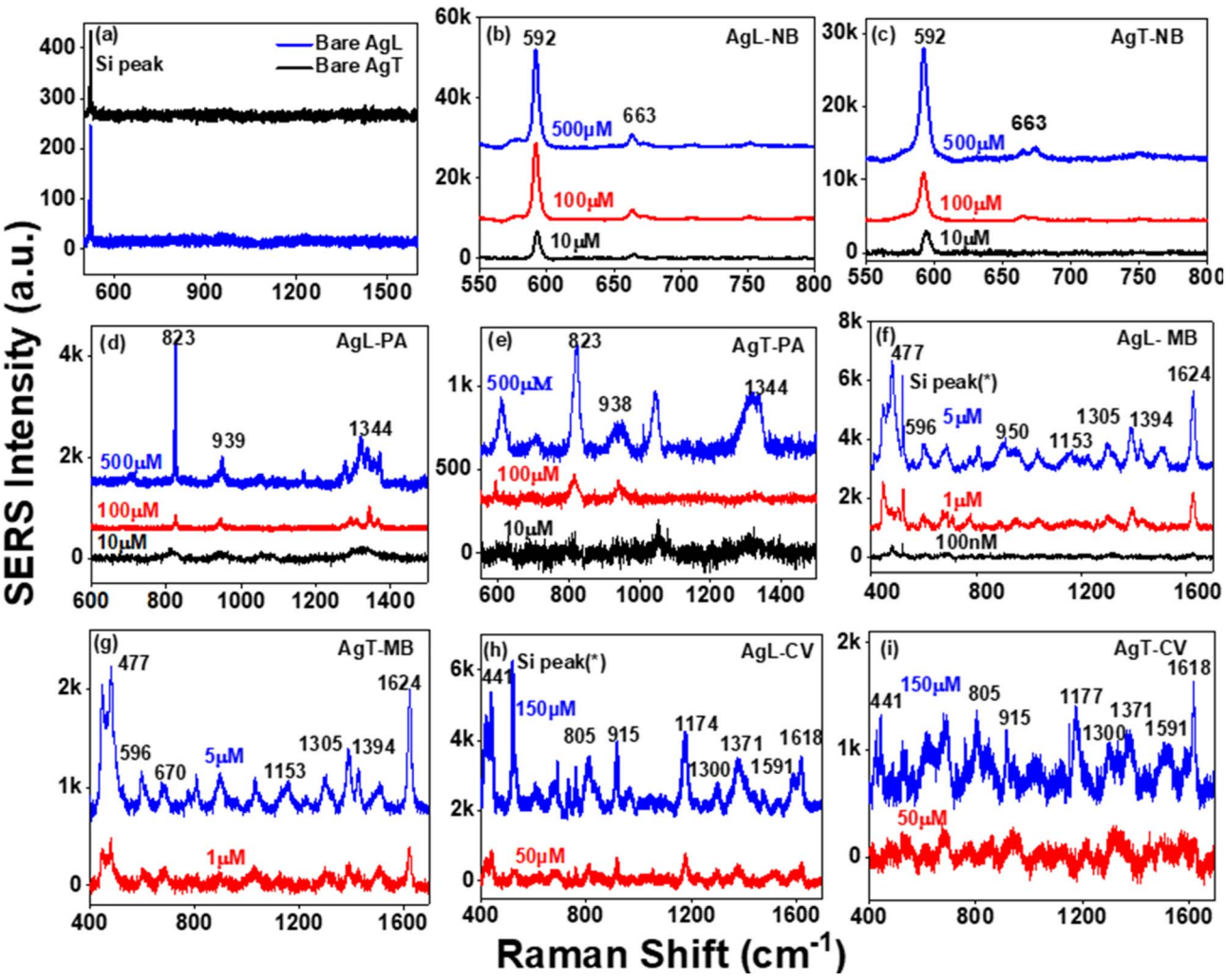

Fig. 5 (a) The SERS spectra of bare AgL and AgT substrates. (b), (d), (f) and (h) The SERS spectra of NB, PA, MB and CV at different concentrations obtained with AgL substrate. (c), (e), (g) and (i) the SERS spectra of the same analytes with AgT substrate. Astrik (*) symbol denotes the peak position of phonon mode of the Si substrate used.

Raman modes of NB consist of an intense mode at 592 cm^{-1} associated with C–C–C and C–N–C deformation and a small Raman peak at 663 cm^{-1} corresponding to the in-plane C–C–C or N–C–C deformations.[46,55] SERS features of NB with AgT as substrate shown similar characteristics as depicted in Fig. 5(c). However, the intensity of 592 cm^{-1} peak is reduced by 66.67%

with AgT substrate and also the peak near 663 cm^{-1} was barely detectable at 10 μM concentration. Furthermore, the detection sensitivity of AgL substrate was investigated for various concentrations of NB ranging from 10 nM to 500 μM. The corresponding variations in SERS intensity with respect to NB concentration is shown in Fig. 6(a). The AgL substrate could detect NB molecules up to a concentration as low as 10 nM. Corresponding statistical analysis of logarithm of SERS intensity to the logarithm of concentration of NB as shown in Fig. 6(b), displaying a linear correlation, with a correlation coefficient (R^2) of 0.98 indicating high reliability of SERS measurements with AgL. A similar linear trend was observed for AgT substrate with a R^2 value of 0.95 with sensitivity only up to 1 μM. The respective graphs denoting the variation of SERS intensity with respect to its concentration and the associated statistical-logarithmic- correlation is shown in Fig. 6(c) and (d), respectively. In the case of PA (500 μM), an explosive molecule, with AgL as SERS substrate has clearly shown the dominant peaks at 823 cm^{-1} associated with C–H bending, another peak observed at 939 cm^{-1} attributed to in-plane C–H bending vibration and 1344 cm^{-1} peak originating from NO_2 symmetric stretching.[47,48] Upon using AgT substrate, the corresponding peaks are observed at lower intensity. Fig. 5(d) and (e) illustrate the SERS spectra of PA measured with AgL and AgT substrates at concentrations 500 μM, 100 μM and 10 μM respectively. With AgT, the intensity of 823 cm^{-1} peak was reduced by 76% at~500 μM, and 1344 cm^{-1} peak was barely detectable at 100 μM concentration. The limits of detection (LODs) of PA were estimated to be 10 μM and 100 μM, respectively, for AgL and AgT substrate.

The SERS measurements of MB analyte were carried out at a concentration of 5 μM, 1 μM and 100 nM. With AgL substrate, as depicted in Fig. 5(f), the signature Raman modes of MB are primarily detected at 445 cm^{-1}/477 cm^{-1} due to deformation of C–N–C skeleton and a peak at 1624 cm^{-1}, originating from C–C ring stretching. Additional secondary peaks are observed at 498 cm^{-1}, 596 cm^{-1}, 670 cm^{-1}, 770 cm^{-1}, 950 cm^{-1}, 1153 cm^{-1}, 1305 cm^{-1} and 1394 cm^{-1}.[49] In contrast, as depicted in Fig. 5(g) the SERS signals with AgT is found to be significantly weak. At 5 μM concentration, the intensity of 1624 cm^{-1} peak is 2.05 times higher for AgL substrate in comparison to AgT substrate. Furthermore, the limit of detection is 100 nM and 1 μM, respectively, for AgL and AgT substrate.

Using CV as probe molecule, at a concentration of 150 μM and 50 μM, the AgL substrate could detect its several characteristic peaks as shown in Fig. 5(h). The peak observed at 441 cm^{-1} corresponding to out of plane vibration of phenyl-C-phenyl, 559 cm^{-1} peak associated with Out-of-plane C–C bending vibration of the aromatic rings, peaks at 729/760 cm^{-1} found to be originating from out-of-plane vibration of ring C–H, and the peaks at 805/915 cm^{-1} due to ring skeletal vibration of radical orientation, the 1174 cm^{-1} peak due to in-plane vibration of ring C–H and 592/1390/1591/1618 cm^{-1} arising from ring C–C stretching.[50] In contrast, AgT substrate Fig. 5(i) displayed only a low intensity distinct peak at 1539 cm^{-1} and a broad band, peak around 1323 cm^{-1} which could be convolution of bands at 1299 cm^{-1} and 1390 cm^{-1}. A detailed assignment to each Raman mode detected with AgL and AgT for each analyte molecule is given in Table 1 of the SI data.

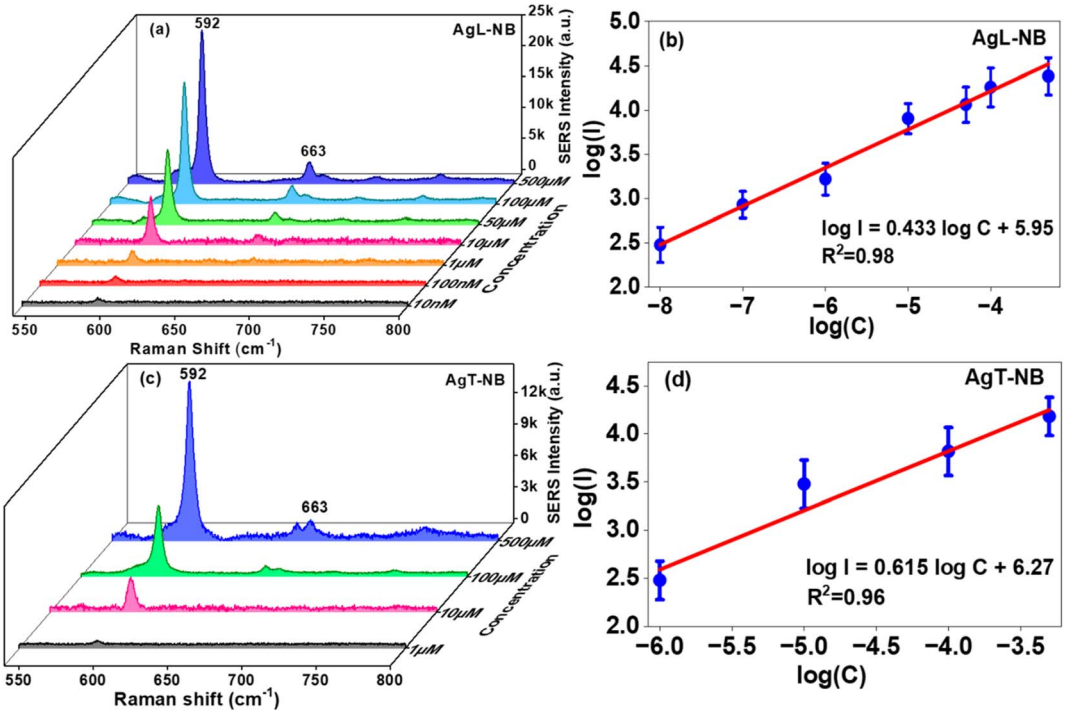

Fig. 6 (a) Concentration-dependent SERS spectra of NB, varying from 10 nM to 500 μM measured using AgL substrate (c) the same measured with AgT for NB concentration varying from 500 μM to 1 μM. (b) and (d) present the graphical variation of logarithmic intensity of 592 cm^{-1} peak of NB *versus* the corresponding logarithmic concentration using AgL and AgT substrate respectively.

4.1 Evaluation of analytical enhancement factor, reproducibility and stability

The Analytical Enhancement Factor (AEF) was estimated using the standard relation $E_F = \left(\frac{I_{SERS}}{I_R}\right)\left(\frac{C_R}{C_{SERS}}\right)$, were I_R, I_{SERS}, C_R, C_{SERS} indicates the Raman signal of analytes with and without SERS substrate as well as analyte concentration with and without SERS substrate.[51] Table 2, represents the AEF calculated for PA, NB, CV and MB respectively. As shown in Table 2, The AEFs were calculated to be 0.86×10^4, 1.2×10^6, 2.7×10^4 and 0.52×10^3 for PA (823 cm^{-1}, 10 μM), NB (592 cm^{-1}, 10 nM), MB (477 cm^{-1}, 100 nM) and CV (1618 cm^{-1}, 50 μM), respectively, with AgL SERS substrate. In contrast, the enhancement factor is measured to be less with AgT substrate, it is one order lesser for NB and MB. This reduced enhancement of AgT can be attributed to non-uniformity in size as well as the shape distributions of NPs of AgT substrate. Moreover, the formation of AgCl phase in AgT NPs may supress its plasmonic properties to considerable extent. By-comparison, AgL possess relatively large nanoparticle density as well as the uniformity in nanoparticle shapes, resulting a comparatively a greater number of hot spots, which is contributing to enhanced SERS signal.

The reproducibility of the substrates was analysed by measuring the SERS spectra randomly from different locations of AgL and AgT substrates. Corresponding intensity variations in signals are depicted as histograms in Fig. 7(a) and (b). The relative standard deviation (RSD), quantifying the reproducibility was estimated to be 13.6%, 14.3%, 5% and 12.6% for NB (592 cm^{-1}), PA (823 cm^{-1}), MB (447 cm^{-1}) and CV (1618 cm^{-1}) respectively with AgL substrate. Contrastingly, the reproducibility is found to be reduced with AgT substrate, the RSD values calculated using the histogram as shown in Fig. 7(b) are 19.3%, 15.9%, 14.1% and 28.8%, respectively, for NB (592 cm^{-1}), PA (823 cm^{-1}), MB (477 cm^{-1}) and CV (1618 cm^{-1}).

Although the dominant contribution to SERS enhancement arises from the induced electromagnetic hotspots, we also examined the role of phytochemical assisted adsorption through zeta potential measurements. Fig. S5 the depicts the zeta potential distribution of AgL and AgT samples with values ~ −19 mV and ~ −15 mV, respectively. A relatively higher negative potential value of AgL compared to AgT indicating a dominant negative surface charge to AgL nanoparticles attributed to the greater abundance of phytochemical capping species in *D. falcata* extract. The strong negative charge of AgL can enhance electrostatic attraction toward cationic ions such as NB, MB, and CV. Consequently, this promotes more effective adsorption on AgL nanoparticles contributing to the effective SERS performance.

Further we have monitored the stability of green AgNPs (both AgL and AgT) using both absorption as well as SERS spectroscopy. Fig. S3(a) and S3(b) depict the absorption spectra of AgL and AgT samples recorded over a time interval of 180 days. The LSPR characteristics of both the samples exhibit only minimal changes during this time. The LSPR peak of AgL is red shifted by 9 nm, while that of AgT by 7 nm, and the LSPR band intensity and width of the samples remain nearly unchanged. The corresponding SERS spectra of the AgL and AgT, shown in Fig. S4(a) and S4(b), also remained consistent during this period. These findings indicate the high stability of synthesized green AgNPs mediated *via D. falcata* and *O. tenuiflorum*.

Table 2 AEF values calculated with AgL and AgT substrates for the probe analytes PA, NB, MB, and CV

Sample	PA [823 cm^{-1}]	NB [592 cm^{-1}]	MB [446 cm^{-1}]	CV [1618 cm^{-1}]
AgL…AEF	0.86×10^4 (10 μM)	1.2×10^6 (10 nM)	2.7×10^4(100 nM)	0.52×10^3 (50 μM)
AgT…AEF	0.5×10^4 (10 μM)	0.1×10^5 (1 μM)	3.19×10^3 (1 μM)	0.17×10^3 (50 μM)

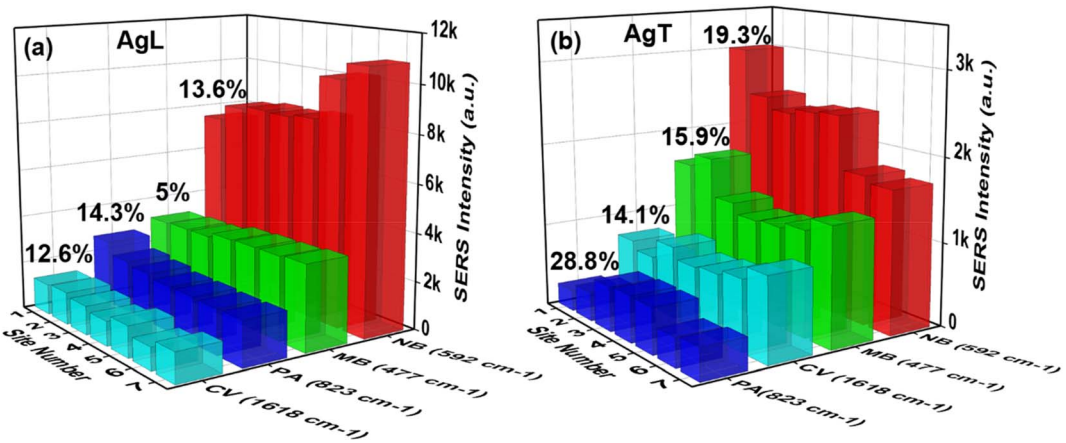

Fig. 7 (a) The histogram plot of the SERS signal of NB (592 cm^{-1}), MB (477 cm^{-1}), PA (823 cm^{-1}) and CV (1618 cm^{-1}) measured from 7 different locations of AgL. (b) Histogram of the same measured with AgT.

4.2 Computational details: dependence of morphology on electric field enhancement factor

In-order to understand the correlation between the nanoparticle morphology to the observed SERS characteristics, the morphological configurations of AgL and AgT NPs [Fig. 8(a) and (b)] were modelled by implementing the finite element method (FEM) by utilizing COMSOL Multiphysics software. The study was conducted in the wavelength domain, aiming to study the effect of nanoparticle morphology on electric field enhancement, which is a key parameter for SERS enhancement. The excitation laser beam (633 nm) was propagating in the *X*-direction and polarized in *Y*-direction. Using a 2D model, morphological configurations of AgL and AgT nanoparticle systems are simulated with reference to TEM images (shown as in-set of Fig. 8). Fig. 8(a) and (b) present the simulated electric field contours of AgT and AgL nanoparticle configuration respectively while 8(c) and 8(d) present the variation in normalized electric field calculated along a line cutting the region of hot spots of AgL and AgT. As illustrated in Fig. 8(a), trimer configuration of non-spherical AgNPs of AgT substrate (with interparticle distance of ~2 nm) exhibited an absolute electric field enhancement of 14-fold. In contrast, the AgL configuration (with interparticle distance of ~1 nm), illustrated in Fig. 8(b), exhibited a significantly stronger enhancement of 20-fold due to formation hotspot region *via* efficient near-field electromagnetic coupling. The Raman Enhancement factor (AEF), which is proportional to the fourth power of the local field factor $\left(\left|\frac{E_0}{E_i}\right|^4\right)$ is estimated to be 1.6×10^5 for AgL and 3.3×10^4 for AgT.[52] The simulated AEF is found to be one order more compared to that of experimental value especially for PA, MB, and CV and this discrepancy may be arising due to the surface chemistry characteristics of green nanoparticles which is not accounted in the COMSOL simulations. The capping agents in green AgNPs may also controls the effective adsorption efficiency of the analyte molecules to the surface of AgNPs. Additionally, formation of AgCl phase in AgT sample further diminishes its plasmonic properties.

Previous studies conducted on the SERS with green AgNPs have primarily focused on the detection of various dye analyte molecules; in-contrast, the present work demonstrates, the detection capability of green AgNPs based SERS substrate for the detection of PA, which is an explosive molecule. For instance, Mazali *et al.* reported the green synthesis of AgNPs using citrus plant extract, which enabled the SERS detection of analytes such as 4-aminobenzenethiol, Rhodamine 6G, and

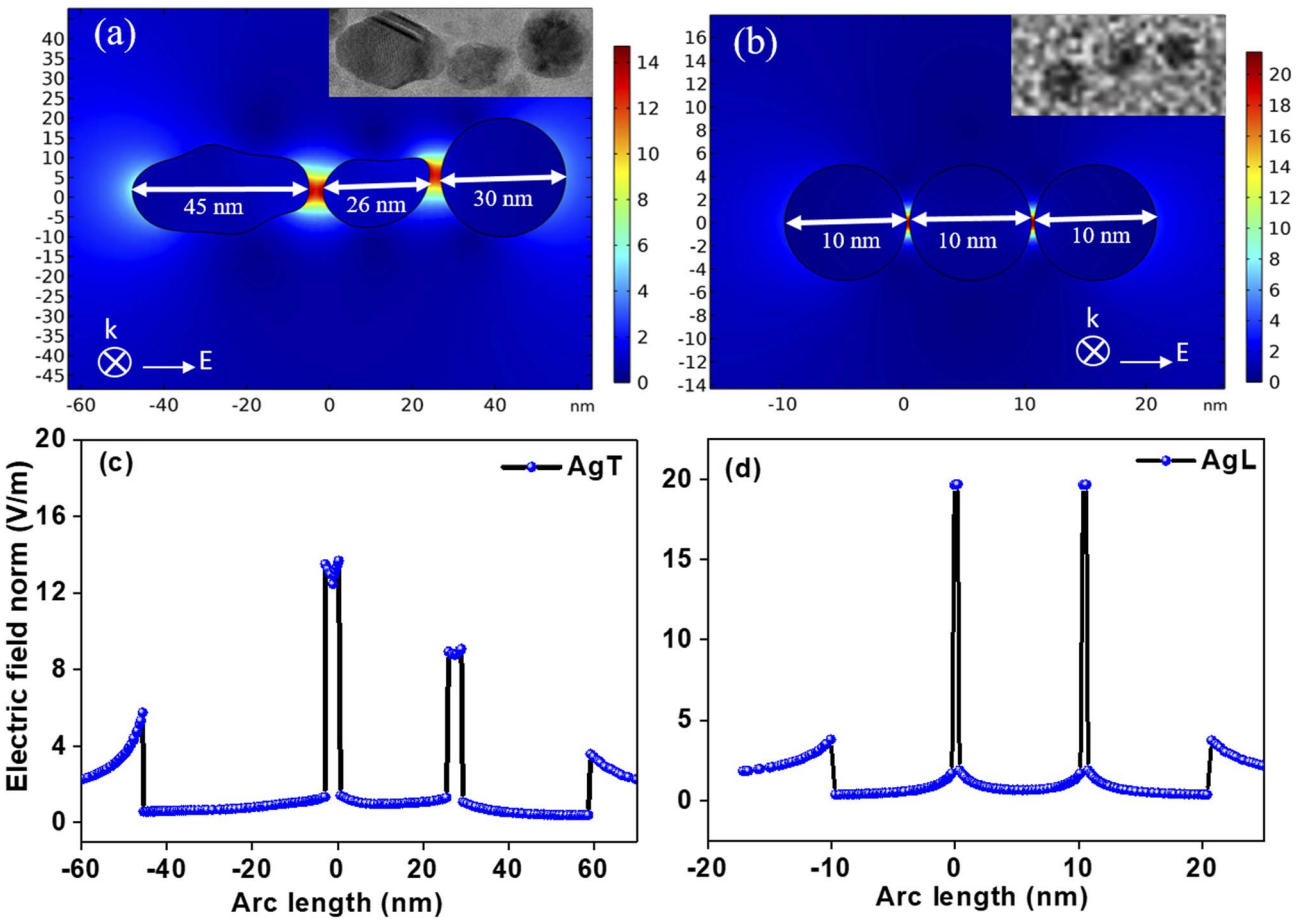

Fig. 8 (a) and (b) Represents the electric-field distribution calculated across the nanoparticle morphology of AgT trimer configuration and normalized electric field calculated along the arc length of AgNPs. (c) and (d) present the same for AgL configuration.

Table 3 The summary of SERS performance of various substrates in comparison to present work. Astrik (*) symbol denotes the concentration reported in the literature not as LOD

		Analyte parameters		
Substrate	Analyte	AEF	LOD	References
AuNPs drop-casted on silicon substrate: laser ablation technique	PA (822 cm^{-1}), MB (1621 cm^{-1})	3×10^4, 1.4×10^6	1 μM, 50 nm	48
AgNPs deposited on periodic-hydrophobic stainless-steel structure: laser ablation technique	PA (1343 cm^{-1})	—	10 μM	58
AgNPs drop-casted on Si substrate/Ag thin film deposited on SiO_2 NPs: chemical synthesis, thermal evaporation method	PA (1282 cm^{-1})	3×10^3, 3.7×10^4	1 μM, 10 μM	59
Colloidal photonic crystal based on AuNPs: emulsion polymerization	PA (1344 cm^{-1}), NB (592 cm^{-1})	—	67 μM, 0.28 nM	60
Ag-hBN nanocomposites drop casted on Si substrate: laser ablation method	NB (590 cm^{-1}), MB (1627 cm^{-1})	—	10 nM, 1 μM	53
Ag@Au Cu@Au bimetallic NPs drop casted on Si substrate: laser ablation method	PA (822 cm^{-1})	4.47×10^4	5 μM	54
Chitosan capped AuNPs: chemical method	NB (590 cm^{-1})	26.85	0.01 mM*	61
AgNPs drop casted on to Si substrate: chemical synthesis	NB-A (1493 cm^{-1})	3.5×10^3	10 μM*	62
Au coated laser patterned nickel surface: laser ablation technique	NB (590 cm^{-1})	8.9×10^5	5 nM	46
AgL based SERS substrate	PA (823 cm^{-1}) NB (592 cm^{-1}) MB (446 cm^{-1})	0.86×10^4 1.2×10^6 2.7×10^4	10 μM 10 nM 100 nM	Present work

Methylene Blue, with detection achieved at 10^{-6} mol L^{-1} concentration. Another study reported the green synthesis of AgNPs using Euphorbia milii leaf extract which detected Crystal violet at concentration of 100 nM.[25,26] Chettri P *et al.* have prepared reduced graphene oxide and AgNP–rGO composites using *Psidium guajava* leaf extract *via* a one-pot reflux method for SERS detection of Methylene blue at 10 nM with an enhancement factor of 4.6×10^5. Aiqin Mao *et al.* synthesized Ag nanocubes using a simple green method by adding NaOH solution to the mixed solutions of $AgNO_3$, glucose and PVP at room temperature and reported a SERS AEF of 5.5×10^4 for crystal violet.[56,57] It is found that the SERS performance of AgL based substrate is comparable with those synthesised using the other methods such as laser ablation technique and chemical synthesis. Table 3 summarizes the comparison of present work with various other SERS substrates available in the literature.

The SERS performance obtained using AgL based substrate exhibited an AEF of the order of 10^4 for PA and 10^6 for NB, which is in comparable with other SERS substrates synthesised using high energy input, assistance of toxic chemicals or sophisticated fabrication technologies. Thus, green AgNPs synthesised using *D. falcata* offers environmentally friendly, low-cost, stable and sustainable green SERS platform that serves as a promising alternative for detecting hazardous explosive and dye molecules. However, to achieve a detection at the single molecular level, there requires an AEF of 10^7, and this can be achieved by incorporating AgL NPs in periodic structures that would provide regions of highly dense hotspots.[51]

5 Femtosecond Z-scan study of AgL and AgT samples

Additionally, a single beam Z-scan technique utilizing femtosecond laser pulses has been implemented to measure the real and imaginary parts of their nonlinear refractive index. In this technique, the sample is translated along a focussed Gaussian beam direction and the corresponding sample transmittance is measured as the function of its position relative to focal plane. In-general one can measure the real and imaginary parts of complex refractive index through closed and open aperture scan simultaneously.[63] The laser parameters used for in this nonlinear measurements are, excitation wavelength, $\lambda \sim 800$ nm, pulse duration, $\tau \sim 50$ fs and the laser was operated at 1 kHz repetition frequency.

Upon exciting the samples (both AgL and AgT) with 800 nm pump, a positive signature of nonlinearity is observed in both closed (CA) as well as in open aperture (OA) scan. Fig. 9(a)–(d) illustrate the CA and OA scans of AgL and AgT samples, respectively. In the CA transmission, the data consists of valley followed by a peak and the OA scan depicted a transmission decrease at focal position. It is proved that under femtosecond laser pulse excitation of silver nanoparticles, the induced nonlinearity originating from hot electron contribution results in an intrinsically positive nonlinearity, which responds in ultrafast time scale.[64,65] For AgL (AgT) sample, the pump laser photons of energy 1.55 eV interact with LSPR band located at

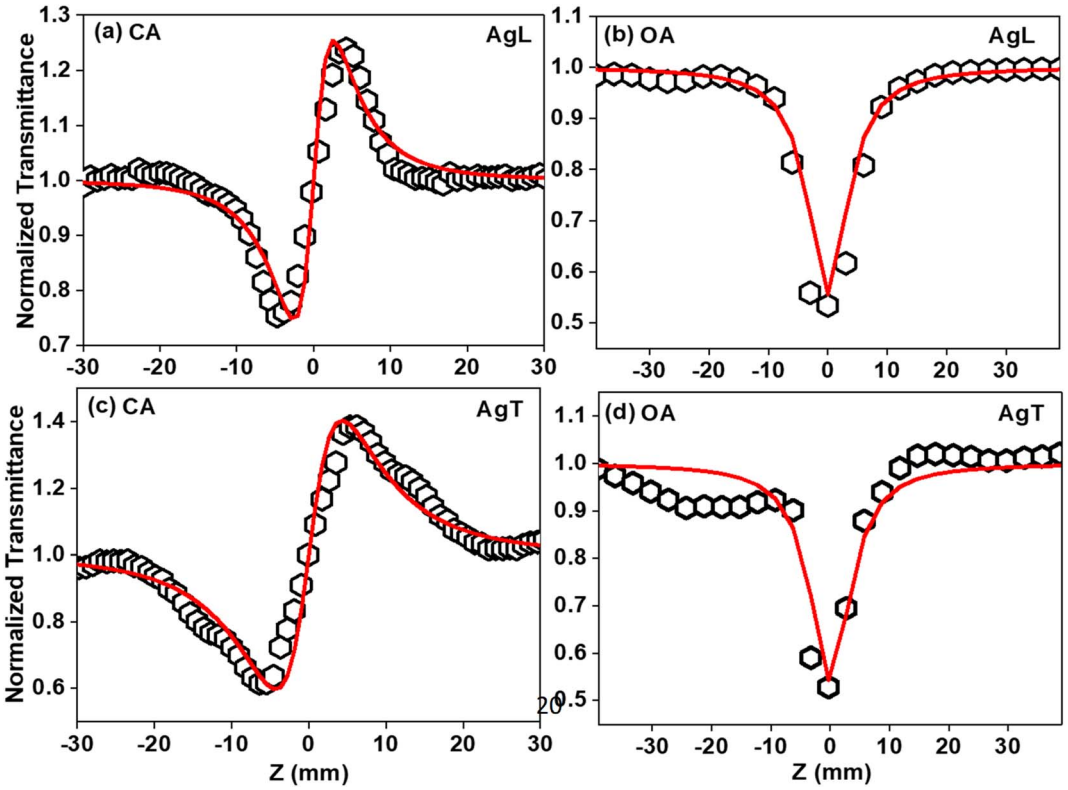

Fig. 9 (a) and (b) Present the CA and OA fs Z-scan data of AgL (c) and (d) presents the same data for AgT samples. Open symbols represent the expeirmental data while the solid (black) lines represent the theoretical fits.

2.94 eV (2.71 eV) through two-photon absorption process. The induced two-photon absorption by an intense laser pulse can be represented by

$$\alpha(I) = \alpha_0 + \beta I$$

where α_0 represents the linear absorption coefficient and β corresponds to the two-photon absorption process. Corresponding fitted values of two-photon absorption coefficient, β for an excitation intensity of 509 GW cm^{-2} were found to be 1.6×10^{-11} cm W^{-1} and 1.7×10^{-11} cm W^{-1}, respectively, for AgL and AgT. An error of ±5% has been estimated for these coefficients arising from input laser pulse fluctuations, fitting errors, error in estimating the beam waist at the focus, *etc.* Whereas the nonlinear refractive index n_2 is evaluated by fitting CA data with the following relation of transmittance

$$T(Z) = 1 + \frac{4(Z/Z_0)\Delta\varphi_0{}^{(3)}}{\left[(Z/Z_0)^2 + 9\right]\left[(Z/Z_0)^2 + 1\right]}$$

where, $T(Z)$ is the normalized transmission of CA Z-scan data and $\Delta\varphi_0{}^{(3)} = \frac{2\pi n_2 I_0 L_{\text{eff}}}{\lambda}$, is the third-order nonlinear phase change of the material. The fitted values nonlinear refractive index (n_2) is found to be ~3.18×10^{-16} cm^2 W^{-1} and ~5.07×10^{-16} cm^2 W^{-1}, respectively, for AgL and AgT. The comparatively higher values of the NLO coefficients associated with AgT can be plausibly attributed to the presence of AgCl phase, leading to formation of Ag–AgCl Schottky type heterojunction interfaces.[66,67] Under femtosecond laser pulse excitation with 800 nm, the hot electrons generated in Ag nanoparticles can possibly transiently injected to the conduction level of AgCl. This interfacial charge separation of hot carriers persists on ultrafast time scale (150 fs), resulting in transient polarization at the interface that contributes to observed increase in nonlinear refraction and absorption in AgT.

In contrast to the SERS measurements, which is highly correlated to microstructure of AgNPs, the NLO coefficients are macroscopic in nature demonstrating similar NLO characteristics for both AgL and AgT samples. In the used excitation regime, the fitted values of nonlinear refractive and absorption coefficients of pure water solvent were found to be 1.8×10^{-12} cm W^{-1} and 3.81×10^{-17} cm^2 W^{-1} respectively. The corresponding CA and OA curves of water are given in Fig. S2(a) and S2(b). The nonlinear coefficients of green AgNPs (both AgL and AgT) is found to be one order higher than that of water and which can be enhanced further by optimizing the concentration of nanoparticles. Thus, NLO studies on AgL/AgT and observed 2 PA process suggest that nanomaterials based on green AgNPs can be a potential candidate to realize the nanophotonic devices for optical limiting and switching applications.

6 Conclusions

The present work highlights the potential of green synthesized silver nanoparticles for SERS and NLO applications. The phytochemical composition of a plant extracts plays a crucial

role in determining the morphology AgNPs which in turn govern the efficiency of SERS applications. Among the investigated samples, AgNPs mediated with the leaf extracts of *D. falcata* plant (AgL) demonstrated its superior functionality as SERS substrate compared to those derived from the leaf extract of *O. tenuiflorum* (AgT). FTIR spectroscopy, XRD and TEM analysis have been implemented to investigate the phytochemical composition of leaf extract, structural and morphological features of synthesized AgNPs. AgL nanoparticles possess uniform shape and narrow size distribution exhibited significantly higher electric field enhancement as confirmed by both experimental SERS measurements and COMSOL simulations. The SERS enhancement along with a highest reproducibility and sensitivity in detection of PA, NB, MB, and CV is observed with AgL in comparison to AgT highlight the importance of choosing suitable plant extract for the synthesis of AgNPs for SERS applications. In addition, the third-order NLO properties of green AgNPs (AgL/AgT) were investigated by employing a femtosecond Z-scan measurements, demonstrating a positive nonlinearity arising from two-photon absorption process. The observed nonlinear properties of the green AgNPs makes them promising candidates for optical limiting and optical switching applications. In this context, the studies will be conducted further to enhance nonlinear characteristics of AgL/AgT will be by tailoring the concentration of AgNPs. In-conclusion our work demonstrates, green synthesized AgNPs, especially those with controlled morphology like AgL, can be a cost effective-ecofriendly-sustainable promising candidate for realizing novel SERS substrates as well as suitable candidates for promising nonlinear optical applications.

Author contributions

Jhansi Mogilipuri: methodology, validation, investigation, data curation, writing—original draft. Sri Lakshmi P. Bhaskar: conceptualization, methodology, validation, synthesis of AgL. Venugopal Rao Soma: conceptualization; validation; resources; review and editing; funding acquisition; supervision. Sabitha Mohan: conceptualization, methodology, validation, investigation, supervision, editing, writing—original draft.

Conflicts of interest

The authors declare no conflicts of interests.

Data availability

All data supporting the findings of this study are available within the article and its supplementary information (SI). Supplementary information: TEM monographs of samples, the table representing values of intensities used for calculation of analytical enhancement factor, closed and open aperture Z-scan curves of water, absorption and SERS spectra recorded during the ageing of samples, zeta potential analysis, table describing the Raman modes along with their assignments for the analytes are included. See DOI: https://doi.org/10.1039/d6ra00003g.

Acknowledgements

Sabitha Mohan would like to acknowledge the funding under the Q-Pragathi project of the Quantum Research Park (QuRP, Award number QP202408), funded by Karnataka Innovation and Technology Society (KITS), K-Tech, Government of Karnataka, India. V.R. Soma acknowledges the financial support from DRDO, India. V.R. Soma also thanks the University of Hyderabad for the Institute of Eminence (IoE) project [UOH/IOE/RC1/RC1-20-016]. The IoE project was granted by the Ministry of Education, Government of India, vide MHRD notification F11/9/2019-U3(A). The authors acknowledge the support and laboratory facilities provided such as micro-Raman instrument for Surface Enhanced Raman Spectroscopy by the DRDO Industry-Academia Centre of Excellence (DIA-COE; formerly ACRHEM), School of Physics, and School of Chemistry for their access to UV-Visible spectrophotometer, Transmission Electron Microscopy and Photoluminescence characterisations for the completion of this work at the University of Hyderabad. The authors thank Indian Science technology and Engineering facilities Map (I-STEM), a program supported by Office of the Principal Scientific Advisor to the Govt. of India for enabling access to COMSOL Multiphysics 6.0 software suite to carry out this study. We acknowledge the Sophisticated Analytical Instrumentation Facility, Mahatma Gandhi University, Kottayam for the PL measurements. We acknowledge Dr T. Geetha (Vimala college, Thrissur) for helpful and informative discussions on the synthesis of samples. We thank Sri Sathya Sai University for Human Excellence for their encouragement and support to complete this work.

References

1 K. L. Kelly, E. Coronado, L. L. Zhao and G. C. Schatz, *J. Phys. Chem. B*, 2003, **107**, 668–677.
2 U. Kreibig and M. Vollmer, *Optical Properties of Metal Clusters*, Springer, Berlin, 1995.
3 C. F. Bohren and D. R. Huffman, *Absorption and Scattering of Light by Small Particles*, Wiley-VCH Verlag GmbH, Weinheim, Germany, 1998.
4 D. D. Evanoff and G. Chumanov, *J. Phys. Chem. B*, 2004, **108**, 13957–13962.
5 E. Petryayeva and U. J. Krull, *Anal. Chim. Acta*, 2011, **706**, 8–24.
6 S. Mohan, J. Lange, H. Graener and G. Seifert, *Opt. Express*, 2012, **20**, 28655–28663.
7 S. Nie and S. R. Emory, *Science*, 1997, **275**, 1102–1106.
8 S. L. Kleinman, R. R. Frontiera, A. I. Henry, J. A. Dieringer and R. P. Van Duyne, *Phys. Chem. Chem. Phys.*, 2013, **15**, 21–36.
9 H. Xu, E. J. Bjerneld, M. Käll and L. Börjesson, *Phys. Rev. Lett.*, 1999, **83**, 4357–4360.
10 R. Beeram, K. R. Vepa and V. R. Soma, *Biosensors*, 2023, **13**, 328.
11 D. Banerjee, M. Akkanaboina, R. K. Kanaka and V. R. Soma, *Appl. Surf. Sci.*, 2023, **616**, 156561.

12 J. Rathod, C. Byram, R. K. Kanaka, M. S. S. Bharati, D. Banerjee, M. Akkanaboina and V. R. Soma, *ACS Omega*, 2022, **7**, 15969–15981.
13 P. Yu, L. Ma, X. Yang, S. Xue, Z. Zhang, L. Sun and J. Cai, *ACS Omega*, 2025, **10**, 25158–25175.
14 D. D. Evanoff, R. L. White and G. Chumanov, *J. Phys. Chem. B*, 2004, **108**, 1522–1524.
15 T. A. Estrada-Mendoza, D. Willett and G. Chumanov, *J. Phys. Chem. C*, 2020, **124**, 27024–27031.
16 R. Gupta and H. Xie, *J. Environ. Pathol. Toxicol. Oncol.*, 2018, **37**, 209–230.
17 A. Sati, T. N. Ranade, S. N. Mali, H. K. A. Yasin and A. Pratap, *ACS Omega*, 2025, **10**, 7549–7582.
18 N. K. Sharma, J. Vishwakarma, S. Rai, T. S. Alomar, N. AlMasoud and A. Bhattarai, *ACS Omega*, 2022, **7**, 27004–27020.
19 M. Fahim, A. Shahzaib, N. Nishant, A. Jahan, T. A. Bhat and A. Inam, *JCIS Open*, 2024, **16**, 100125.
20 S. Shahzadi, S. Fatima, Qurat ul ain, Z. Shafiq and M. R. S. A. Janjua, *RSC Adv.*, 2025, **15**, 3858–3903.
21 S. Raza, M. Wdowiak, M. Grotek, W. Adamkiewicz, K. Nikiforow, P. Mente and J. Paczesny, *Nanoscale Adv.*, 2023, **5**, 5786–5798.
22 T. S. Rashid, Y. Galali, H. K. Awla and S. M. Sajadi, *Results Chem.*, 2024, **11**, 101849.
23 N. M. Alassadi, J. Ghaida'a, A. M. Amshawee and R. Ali, *Next Nanotechnol.*, 2025, **8**, 100275.
24 W. A. Shaikh, S. Chakraborty, G. Owens and U. R. Islam, *Appl. Nanosci.*, 2021, **11**, 2625–2660.
25 E. B. Santos, N. V. Madalossi, F. A. Sigoli and I. O. Mazali, *New J. Chem.*, 2015, **39**, 2839–2846.
26 V. Dixit, R. Rahmathulla, T. P. Kulangara, S. Thirunavukkuarasu, V. Kumar and D. Jaiswal-Nagar, *Microchem. J.*, 2025, **213**, 113611.
27 S. Horta-Pineres, M. Cortez-Valadez, D. A. Avila, J. E. Leal-Perez, A. Hurtado-Macias, M. Flores-Acosta and C. O. Torres, *Appl. Phys. A*, 2022, **128**, 1090.
28 A. Hakonen, F. C. Wang, P. O. Andersson, H. Wingfors, T. Rindzevicius, M. S. Schmidt, V. R. Soma, S. Xu, Y. Li, A. Boisen and H. Wu, *ACS Sens.*, 2017, **2**, 198–202.
29 S. Mehra, M. Singh and P. Chadha, *Toxicol. Int.*, 2021, **28**, 165.
30 D. Kong, L. Wang, Y. Niu, L. Cheng, B. Sang, D. Wang, J. Tian, W. Zhao, X. Liu and Y. Chen, *Front. Pharmacol.*, 2023, **14**, 1096379.
31 S. P. Pattanayak and P. Sunita, *J. Ethnopharmacol.*, 2008, **120**, 241–247.
32 M. S. Baliga, R. Jimmy, K. R. Thilakchand, V. Sunitha, N. R. Bhat, E. Saldanha, S. Rao, P. Rao, R. Arora and P. L. Palatty, *Nutr. Cancer*, 2013, **65**(Suppl. 1), 26–35.
33 M. Z. Ahmad, M. Ali, S. R. Mir and J. Pharmacogn, *Phytother.*, 2012, **4**, 75–85.
34 A. D. Sharma, I. Kaur, S. Angish, A. Thakur, S. Sania and A. Singh, *BioTechnologia*, 2022, **103**, 131.
35 S. P. Bhaskar and A. Anto, *Chem. Pap.*, 2023, **77**, 6859–6871.
36 M. H. Ali, M. A. K. Azad, K. A. Khan, M. O. Rahman, U. Chakma and A. Kumer, *ACS Omega*, 2023, **8**, 28133–28142.
37 N. Thirumagal and A. P. Jeyakumari, *J. Clust. Sci.*, 2020, **31**, 487–497.
38 K. Okaiyeto, M. Ojemaye, H. H. Hoppe, L. V. Mabinya and I. A. Okoh, *Molecules*, 2019, **24**, 4382–4397.
39 Z. R. Tóth, S. K. Maity, T. Gyulavári, E. Bárdos, L. Baia, G. Kovács, S. Garg, Z. Pap and K. Hernadi, *Catalysts*, 2021, **11**, 379.
40 S. Pasieczna-Patkowska, M. Cichy and J. Flieger, *Molecules*, 2025, **30**, 684.
41 N. T. K. Thanh, N. Maclean and S. Mahiddine, *Chem. Rev.*, 2014, **114**, 7610–7630.
42 H. Singh, M. F. Desimone, S. Pandya, S. Jasani, N. George, M. Adan, A. Aldarhami, A. S. Bazaid and S. A. Alderhami, *Int. J. Nanomed.*, 2023, **18**, 4727–4750.
43 O. A. Yeshchenko, I. M. Dmitruk, A. A. Alexeenko, M. Y. Losytskyy, A. V. Kotko and A. O. Pinchuk, *Phys. Rev. B: Condens. Matter Mater. Phys.*, 2009, **79**, 235438.
44 S. Vankudoth, S. Dharavath, S. Veera, N. Maduru, R. Chada, P. Chirumamilla, C. Gopu and S. Taduri, *Biochem. Biophys. Res. Commun.*, 2022, **630**, 143–150.
45 M. Lang, F. Stober and H. K. Lichtenthaler, *Radiat. Environ. Biophys.*, 1991, **30**, 333–347.
46 B. Chandu, M. S. S. Bharati, P. Albrycht and S. V. Rao, *Opt. Laser Technol.*, 2020, **131**, 106454.
47 S. S. B. Moram, C. Byram and V. R. Soma, *Bull. Mater. Sci.*, 2020, **43**, 53.
48 C. Byram, S. S. B. Moram, A. K. Shaik and V. R. Soma, *Chem. Phys. Lett.*, 2017, **685**, 103–107.
49 T. T. H. Pham, X. H. Vu, N. D. Dien, T. T. Trang, T. T. K. Chi, P. H. Phuong and N. T. Nghia, *RSC Adv.*, 2022, **12**, 7850–7863.
50 R. Mandavkar, S. Lin, S. Pandit, R. Kulkarni, S. Burse, M. A. Habib, S. Kunwar and J. Lee, *Surf. Interfaces*, 2022, **33**, 102175.
51 E. C. Le Ru, M. Blackie, M. Meyer and P. G. Etchegoin, *J. Phys. Chem. C*, 2007, **111**, 13794–13803.
52 E. C. Le Ru and P. G. Etchegoin, *Chem. Phys. Lett.*, 2006, **423**, 63–66.
53 K. Bera, S. S. B. Moram, D. Banerjee, J. Lahiri and V. R. Soma, *Opt. Mater.*, 2024, **157**, 116393.
54 S. S. B. Moram, C. Byram and V. R. Soma, *Front. Phys.*, 2018, **6**, 28.
55 C. Byram, J. Rathod, S. S. B. Moram, A. Mangababu and V. R. Soma, *Nanomaterials*, 2022, **12**, 2150.
56 P. Chettri, V. S. Vendamani, A. Tripathi, M. K. Singh, A. P. Pathak and A. Tiwari, *Appl. Surf. Sci.*, 2017, **406**, 312–318.
57 A. Mao, X. Jin, X. Gu, X. Wei and G. Yang, *J. Mol. Struct.*, 2012, **1021**, 158–161.
58 S. Mangalassery, N. Chaudhary and S. R. G. Naraharisetty, *Surf. Interfaces*, 2023, **42**, 103454.
59 N. Mazur, V. Dzhagan, O. Kapush, O. Isaieva, P. Demydov, V. Lytvyn, V. Chegel, O. Kukla and V. Yukhymchuk, *RSC Adv.*, 2025, **15**, 252–260.
60 S. Narayanan, J. Rathod, V. R. Soma and B. V. R. Tata, *Nano Futures*, 2025, **9**, 015001.
61 H. B. da Silva, L. P. D. F. Peixoto and G. F. S. Andrade, *Plasmonics*, 2025, **20**, 7705–7714.

62 T. L. Hoang, H. V. Pham and M. T. T. Nguyen, *J. Electron Mater.*, 2019, **49**, 1864–1871.
63 M. Sheik-Bahae, A. A. Said, T. H. Wei, D. J. Hagan and E. W. Van Stryland, *IEEE J. Quantum Electron.*, 2003, **26**, 760–769.
64 F. Hache, D. Ricard, C. Flytzanis and U. Kreibig, *Appl. Phys. A*, 1998, **47**, 347–357.
65 M. Guillet, M. Rashidi-Huyeh and B. Palpant, *Phys. Rev. B: Condens. Matter Mater. Phys.*, 2009, **79**, 045410.
66 Y. Tang, Z. Jiang, G. Xing, A. Li, D. P. Kanhere, Y. Zhang, C. T. Sum, S. Li, X. Chen, Z. Dong and Z. Chen, *Adv. Funct. Mater.*, 2013, **23**, 2932–2940.
67 P. Zhang, C. Wang and D. Yu, *Thin Solid Films*, 2024, **803**, 140470.